High-speed two-color scanning volumetric laser-induced fluorescence

Diega Tapia Silva
University of California, Merced
Cole J. Cooper
University of California, Merced
Tracy L. Mandel
University of New Hampshire
Shilpa Khatri
University of California, Merced
Dustin Kleckner (dkleckner@ucmerced.edu)
University of California, Merced

Research Article

Keywords: Imaging techniques, 3D imaging, high-speed imaging, laser-induced fluorescence, VLIF

Posted Date: June 7th, 2023

DOI: https://doi.org/10.21203/rs.3.rs-2977609/v1

Additional Declarations: No competing interests reported.

High-speed two-color scanning volumetric laser-induced fluorescence

Diego Tapia Silva[1], Cole J. Cooper[1], Tracy L. Mandel[2], Shilpa Khatri[3] and Dustin Kleckner[1*]

[1]Department of Physics, School of Natural Sciences, University of California, Merced, 5200 Lake Rd, Merced, 95343, CA, United States of America.
[2]Department of Mechanical Engineering, Center for Ocean Engineering, University of New Hampshire, 24 Colovos Rd, Durham, 03824, NH, United States of America.
[3]Department of Applied Mathematics, School of Natural Sciences, University of California, Merced, 5200 Lake Rd, Merced, 95343, CA, United States of America.

*Corresponding author(s). E-mail(s): dkleckner@ucmerced.edu;
Contributing authors: dtapiasilva@ucmerced.edu; ccooper@ucmerced.edu; tracy.mandel@unh.edu; skhatri3@ucmerced.edu;

Abstract

Many problems in fluid mechanics require single-shot 3D measurements of fluid flows, but are limited by available techniques. Here, we design and build a novel flexible high-speed two-color scanning volumetric laser-induced fluorescence (H2C-SVLIF) technique capable of simultaneous measurement of 3D velocity fields and a secondary tracer in the flow. This is paired with a custom, open source, software package, which allows for real time playback with correction of perspective defects while simultaneously overlaying arbitrary 3D data. The technique is demonstrated with two experiments: (1) the flow past a sphere, and (2) vortices embedded in laminar pipe flow. In the first experiment, two channel measurements are taken at a resolution of 512 × 512 × 512 with volume rates of 65.1 Hz. In the second experiment, a single color SVLIF system is integrated on a moving stage, providing imaging at 1280 × 304 × 256 with volume rates of 34.8 Hz. Although

this second experiment is only single channel, it uses identical software and much of the same hardware to demonstrate the extraction of multiple information channels from single channel volumetric images.

Keywords: Imaging techniques, 3D imaging, high-speed imaging, laser-induced fluorescence, VLIF

1 Introduction

Progress in experimental fluid mechanics is often limited by techniques for measuring flow fields (Tropea et al (2007)). This is especially true for chaotic flows – such as turbulence – which necessitate single shot 3D measurements (Wu et al (2015); Ma et al (2017)). In recent decades, high-speed imaging has been made possible through the development of low light high-speed cameras, high-speed scanning mirrors and the development of mass data processing techniques (Versluis (2013)). The development of the digital camera resulted in experimental two-dimensional imaging techniques such as planar laser-induced fluorescence (PLIF), particle imaging velocimetry (PIV), and particle tracking velocimetry (PTV). PLIF works by shining a laser sheet through a fluid sample that is embedded with a fluorescent tracer (Hammack et al (2018); Zhu et al (2019)). The fluorescent signal that arises from the laser sheet exciting the tracer is then captured by a camera. PIV and PTV rely on imaging a fluid sample that is embedded with particle tracers (Bryanston-Cross and Epstein (1990); Palafox et al (2007); Adamczyk and Rimai (1988); Brücker and Althaus (1992)).

Traditionally, imaging of fluid dynamics has been restricted to planar investigations. However, fluids flows are intrinsically three-dimensional, and hence to experimentally capture the full dynamics volumetric imaging is necessary. For example, planar imaging techniques have been widely applied to study the flow dynamics of animals (Katija et al (2015); Pepper et al (2015); Samson et al (2019)). In one study, volumetric PIV imaging was applied to study hydrodynamics of a shark tail (Flammang et al (2011)), leading to qualitatively different results than previous work using planar PIV on the wake structures (Wilga and Lauder (2002, 2004)). In this particular case a dual-ring vortex structure shed from the tails could not be fully resolved from the planar measurements alone, leading to an incorrect interpretation of the overall flow structure. Similarly, in the study of turbulence intrinsically 3D mechanisms like vortex stretching can not be resolved from planar measurements alone (Ouellette (2012)).

PIV, PTV and PLIF can be extended to three-dimensional imaging. One approach is to integrate a system of multiple cameras, or stereoscopes, to capture unique viewing angles enabling the reconstruction of volumes from the various viewing perspectives. This approach is implemented in tomographic particle image velocimetry (TPIV) (Ortiz-Dueñas et al (2010)), tomographic

particle tracking velocimetry (TPTV) (Cornic et al (2020)) and tomographic laser-induced fluorescence (TLIF) (Meyer et al (2016)). An alternative is to image *volumes* of the fluid by sectioning slices of the sample with a laser sheet that is scanned in time (Krug et al (2014)). This approach is used in scanning volumetric laser induced fluorescence (SVLIF); it has the benefit of simpler hardware (i.e. a single camera) and much simpler post-processing of the resulting data. Recent technological developments – e.g. imaging hardware and mass data processing techniques – now make it possible to achieve high spatial and temporal resolutions in volumetric imaging (Shi et al (2018); Osborne et al (2016)).

Through careful considerations of the fundamental and practical limits to high-speed volumetric imaging, here we develop a high-speed two-color scanning volumetric laser-induced fluorescence (H2C-SVLIF) imaging system which operates at the limit of available technology. Although other volumetric two-color techniques have been demonstrated in the past (Halls et al (2018)), our imaging technique is the first, high-speed two-color scanning technique operating at video rates or faster, $\gtrsim 30$ Hz. As a proof of concept, we conduct H2C-SVLIF measurements for a set of experiments: (1) flow past a sphere, and (2) vortices embedded in pipe flow. In the first of the experiments, we use two separate fluorescent dyes excited by a pair of pulsed lasers to simultaneously track small tracer particles and dyed volumes of fluid. In the second case we extract two separate data channels – a velocity field reconstructed from tracer particles and the high resolution dyed vortex lines – using geometric identification of these two features. The set of experiments use identical software and nearly identical hardware, demonstrating the flexibility of our technique. The data collection, data processing, and data visualization are easily expedited using our own novel custom open source software (Kleckner (2021b)). This software has the ability to correct for perspective effects in real time while simultaneously overlaying arbitrary 3D data (e.g. the location of tracked particle or dyed lines).

The outline of this paper is as follows: Section 2 presents the basic design and experimental hardware used in our imaging system, Section 3 discusses the fundamental and practical limits to H2C-SVLIF, Section 4 addresses challenges posed by processing large data sets and how our open source in-house viewing software is adapted to handle these data sets. In Section 5, we discuss the post-processing for distortion correction and calibration for the captured volumes and in Section 6, we discuss the process for the tracking of the particles and the interpolation method for the reconstruction of a Eulerian velocity field. In Section 7, we present results from our example systems, followed up by the conclusion in Section 8.

2 Imaging hardware

The H2C-SVLIF system includes a laser sheet generator, a high-speed camera (*Phantom* V2512), and a custom-designed synchronization board. This board

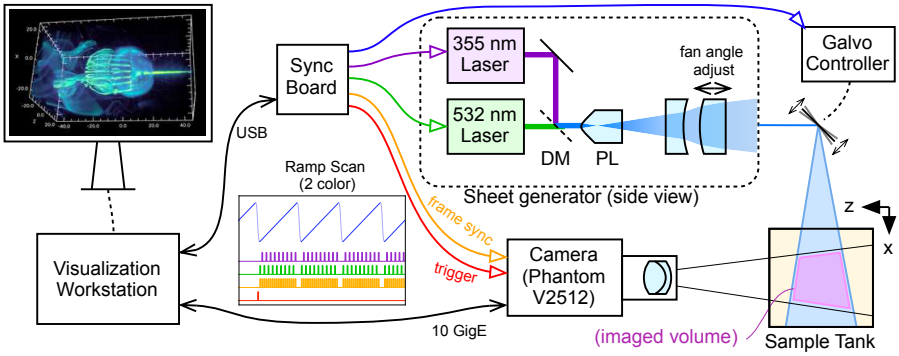

Fig. 1 A schematic of the H2C-SVLIF control system. The entire setup is synchronized using a custom designed board controlled through a GUI in the visualization workstation. The synchronization board generates signals which are sent to the lasers (purple and green), the galvanometer (blue), and high-speed camera (yellow and red). Details of the laser sheet generator are given in Fig. 2.

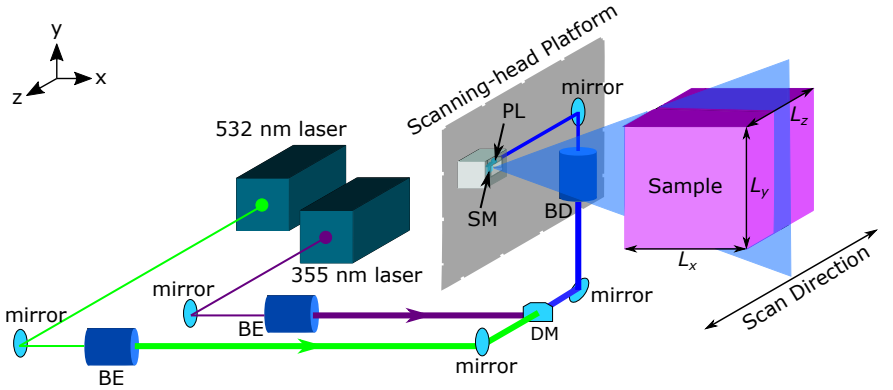

Fig. 2 A schematic of the laser sheet generator. The laser sheet is produced via a pair of pulsed ND: YAG lasers of wavelengths 532 nm and 355 nm. The laser beams pass through a pair of beam expanders (BE). The beams then travel to a dichroic mirror (DM) which combines the beams. From there, the beams get deflected up to a scanning-head platform and pass through a beam de-expander (BD). The scanning-head platform can be manually translated to adjust to a variety of sample heights. Finally, the beams get deflected into the Powell lens (PL) and into the scanning mirror (SM). The resulting laser sheet is then swept across a sample.

– which is controlled through a visualization workstation – synchronizes the camera and laser sheet generator (Fig. 1). To image in three dimensions, the laser sheet is swept across the sample while the high-speed camera records the fluorescent emission slices of the sample. The system is designed to be highly adjustable: the scan width and height are adjustable to image systems at a variety of scales.

The scanning laser sheet is generated by a mobile integrated platform, allowing the position and height of the laser sheet to be easily adjusted (Fig. 2). The laser sources for the sheet are a pair of diode-pumped lasers (*Spectra*

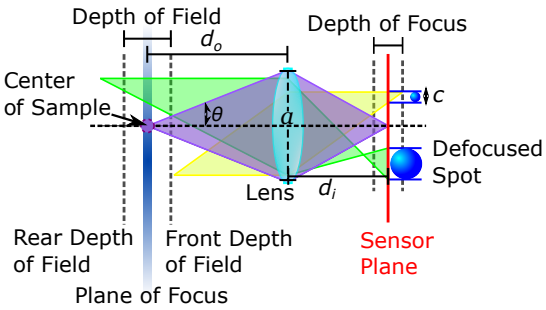

Fig. 3 Schematic of the focusing optics of the camera. The defocused spot size occurs for distances outside the depth of field, d_{field}. The permissible circle of confusion, c, occurs at the rear and at the front depth of field. The maximum lens aperture size, a, depends on the sample angle, θ. Here, d_o and d_i are the distance to object and distance to image respectively.

Physics Explorer One XP 532 and Explorer One XP 355-2). The beams are first expanded to 3 mm, and then combined on a dichroic mirror and directed vertically to the scanning head platform. The head has a manually adjustable height; the 3 mm width of the lasers in the vertical beam section ensures that the divergence of the beams is small enough that this does not significantly affect the beam size over the range of accessible heights. The beams are then de-expanded to the appropriate diameter for the Powell lens (1 mm), which spreads the laser into a uniform vertical sheet. (If needed, the collimation adjustment on the final beam expander can be used to adjust the focus of the final sheet.) Finally, the laser is reflected off a galvonometer mirror (*Thorlabs* GVS001) and directed to the sample.

The high-speed camera, galvanometer, and the lasers are synchronized using the custom designed synchronization board; schematics for this board are publicly available on GitHub (Kleckner (2021a)). This board sends an analog sawtooth signal to the galvanometer controller to define the scanned volume; this can be adjusted in software as needed. A pair of digital pulse signals are sent to the pulsed lasers to excite fluorescence at different wavelengths on alternating frames. A digital frame sync signal is sent to the camera to trigger synchronized acquisition. A second trigger signal is sent to the camera to designate the start of the first recorded volume. This entire setup is controlled through a visualization workstation connected to the synchronization board through a USB connection. The camera is also connected to the workstation through a 10 Gb ethernet port, allowing for fast download of large data sets.

3 Fundamental and practical limits to high-speed volumetric imaging

There are limits to the resolution, speed, and signal-to-noise ratio of a volumetric imaging system. These limits may either be fundamental physical constraints (diffraction and shot noise) or practical hardware limitations (camera speed, sensitivity, and data storage). We discuss each of these below, and

arrive at practical limits for high-speed volumetric imaging with the currently available hardware.

3.1 Image resolution

Ideally, the laser sheet would maintain the same thickness throughout the sample, but in practice this is limited by diffraction. Although we are only focusing the laser sheet along a single axis, the beam parameters can still be computed with standard Gaussian optics (Siegman Anthony E (1986)), assuming the source laser has a Gaussian profile (as is the case for the lasers used in our sheet generator). A reasonable balance between the thickness of the sheet and the distance over which it is focused can be obtained by setting the Rayleigh length, $z_R = \frac{n_s \pi w_0^2}{\lambda}$, to be half of the sample size in the direction of laser travel, L_x (Fig. 2), where n_s is the index of refraction of the sample, w_0 is the waist of the Gaussian beam, and λ is the vacuum wavelength of the laser.

To ensure uniform sampling, we set the depth of a single voxel to be equal to the the full width half maximum (FWHM) of the laser sheet. This results in a voxel size $h_{z,dl} = w_0\sqrt{2\ln 2} = \sqrt{\frac{\lambda \ln 2}{\pi n_s L_x}}$. This should be regarded as the maximum useful resolution; higher resolutions would result in a negligible increase in information in the measured volume. Although the resolution limits above were based on the laser sheet, the same fundamental limits apply to the camera system and corresponding lens, i.e. $h_{x,dl} = h_{y,dl} = \sqrt{\frac{\lambda \ln 2}{\pi n_s L_z}}$. Table 1 shows the diffraction limited resolutions as a function of sample size.

Table 1 The diffraction limited resolutions for cubic volumes, for the 532 nm wavelength laser and the 355 nm wavelength laser, and an index of refraction of the sample, $n_s = 1.33$, for water.

λ (nm)	$L_x = L_y = L_z$ (mm)	$h_{z,dl}$ (mm)	$N_{z,dl}$
532	500	0.148	2380
	250	0.115	1680
	100	0.094	1060
	50	0.067	753
355	500	0.172	2910
	250	0.012	2060
	100	0.077	1300
	50	0.054	921

For large volume sizes, $L_z \gtrapprox 100$ mm, the diffracted limited resolution, $N_{x,dl}$, exceeds the image resolutions of commonly available high-speed cameras. As a result, it is sometimes desirable to under-resolve the image. This brings additional benefits as it allows for an increase in the physical size of the

aperture in the camera, which corresponds to a brighter image for the same amount of laser power. Provided our desired image resolution, N_x, is lower than the diffracted limited resolution $N_{x,dl}$, we can approximate the defocusing with a ray optics approach (Ward and Jacobson (2000)). Here we define an F-number for the lens aperture: $F = f/a$, where a is the aperture diameter and f is the focal length. (Note that per our definition, $F = 8$ corresponds to 'f/8', as it is usually specified on camera lenses.) To compute the acceptable lens aperture, we will set the 'circle of confusion' (the size of a defocused spot at the edge of the volume) to $c = 2p$, where p is the pixel pitch on the camera sensor ($p = 28$ μm for the Phantom V2512). If we then require that the depth of field be equal to L_z, we can obtain:

$$F = \frac{M^2 L_z}{2 n_s c} = \frac{p L_z}{4 n_s h^2} \tag{1}$$

where $M = p/h$ is the image magnification, and h is the size of a voxel along the x or y axis at the center of the imaged volume. The correction due to the sample index of refraction, n_s, can be computed using a ray transfer matrix (Gerrard and Burch (1994)).

3.2 Image intensity

In order to obtain an image with good signal to noise ratio, we need to ensure a sufficient amount of light reaches the image sensor. Electronic camera sensors work by converting incoming photons to electrons, which are then amplified and digitized. The number of electrons per pixel read by the sensor is given by $n_e = \eta n_\gamma$, where η is the quantum efficiency ($\eta \approx 0.4 - 0.95$ for modern sensors (Janesick (2007)) and n_γ is the number of photons which reach a single pixel in each image exposure. In practice the two relevant sources of noise are technical readout noise and shot noise which comes from the fact that electrons are quantized. The technical readout noise is typically referred to as the dark noise and measured in terms of number of electrons, n_d, and the quantum mechanical shot noise is due to relative flucations of photons hitting the sensor and has an amplitude of $\sqrt{n_e}$ (Janesick (2007)). Assuming these are the only sources of noise, the signal to noise ratio is given by $SNR = n_e/\sqrt{n_d^2 + n_e}$. Although n_d can be as low as 1 electron for high sensitivity SCMOS or CCD cameras, it is approximately of order $n_d \approx 10 - 20$ electrons for high-speed cameras (Gilroy and Lucatorto (2019)). If we assume $\eta = 0.5$ and $n_\gamma = 1000$ photons/pixel, $SNR \approx 20$. Note that this is primarily limited by quantum efficiency and shot noise, and so a lower noise camera would produce only marginally better results (a *perfect* camera with $\eta = 1$ and no excess noise would produce $SNR \approx 30$). In the following discussion we will use $n_\gamma = 1000$ photons/pixel as the reference level of intensity; in practice this produces satisfactory images for later analysis.

We image samples by seeding them with a fluorescent dye which is excited by the laser sheet. If we wish to produce n_γ photons per pixel, the required

energy in a single laser pulse, assuming the small angle approximation, is given by,

$$E_{pulse} = \frac{N_y n_\gamma E_\gamma}{\gamma \eta_{opt}} \left(\frac{4\pi}{\pi \theta^2} \right) = \frac{N_y n_\gamma E_\gamma}{\gamma \eta_{opt}} \left(\frac{4 n_s F}{M} \right)^2, \tag{2}$$

where E_{pulse} is the laser pulse energy, $E_\gamma = h_p c/\lambda \approx 4 \times 10^{-19}$ J is the energy of a single photon (h_p is the Planck constant, c is the speed of light, and we have computed the energy for $\lambda = 500$ nm), $\eta_{opt} \approx 0.5$ is the overall optical efficiency of the system (including the quantum yield of the dye and any other optical sources of loss), $\theta = \frac{M}{2 n_s F}$ is the sample half-angle (Fig. 3), γ is the extinction coefficient of a single voxel which is fully dyed, and N_y is the image resolution in the vertical direction. The term in parenthesis is the fractional solid angle of light collected by the camera lens. For situations where the majority of the sample is dyed, we require $\gamma \ll 1/N_x$ to prevent significant shadowing effects.

Let us consider a reference case, where we are imaging a cubic volume of size $L_x = L_y = L_z = 100$ mm, filled with water ($n_s = 1.33$), and pumped with a 532 nm laser. If we use the diffraction limited resolution ($N_{dl} = 1060$) for the image resolution and have a pixel size of $p = 28$ μm, we obtain $M = 0.297$. The corresponding aperture size per (1) is $F \approx 59$ (assuming $n = 1.33$). If we assume an extinction coefficient of $\gamma = 0.1/N_x \approx 10^{-4}$, and a peak imaging brightness of $n_\gamma \approx 1000$, the required pulse energy is ≈ 10 mJ, which is around 100 times more power than is produced by common pulsed lasers with a sufficiently high repetition rate of $\approx 10^4 - 10^5$ Hz (HONG et al (2001)).

This reference case suggests a practical limitation: when imaging macro-scale objects, the resulting large F-number and small magnification will necessitate a large energy per pulse. In this case, a significant improvement can be made by under-resolving the image, and increasing the camera aperture so that the resolution is limited by the depth-of-field of the lens, as described in Section 3.1. A decrease in the resolution will result in bigger spot sizes of the permissible circle of confusion, and will in turn correspond to a larger half-angle of the imaging sample, scaling as $\theta \propto 1/N_z$.

As an example, suppose we reduce the resolution to $N_x = N_y = N_z = 500$. In this case we can decrease the magnification to $M = 0.140$, and increase the aperture size so that $F \approx 15$. Furthermore, let us assume that only a small fraction of the sample is dyed, then we can increase the dye density so that $\gamma = 1/N_x$. Taking into account all of these modifications, the resulting energy required per pulse is $E_{pulse} \approx 65$ μJ. If we are recording volumes at a rate of 60 Hz, this is an average power of 2 W, which is achievable with commonly available lasers.

3.3 Volumetric recording rate

The volumetric acquisition rate of our H2C-SVLIF imaging system is limited by the sweeping rate of the galvanometer and the resolution of the high-speed

camera. At low resolutions, the volumetric acquisition rate will approach the maximum sweeping rate of the galvanometer motor. For a sawtooth signal the maximum sweeping rate at full scale bandwidth for our galvanometer is 175 Hz.

At high resolutions, the volumetric acquisition rate is limited by the throughput of the high-speed camera. Due to the finite speed of the galvanometer, it will produce a smooth linear ramp during a fraction of the total scan time, known as the duty cycle, η_d. The duty cycle depends on the volume scan rate and the speed at which the galvanometer can reset and stabilize. The camera recording signal is synchronized with the effective scan period to only record during this period. The following equation is used to compute the volume rate of the system when limited by the throughput of the camera,

$$r_v = \frac{r_f \eta_d}{N_c N_z} \tag{3}$$

where r_v is the volumetric acquisition rate, r_f is the frame rate of the camera, and N_z is the resolution in the scanning depth direction, and N_c is the number of channels. The maximum volumetric aquisition rate is summarized in Table 2.

Table 2 The maximum volumetric acquisition rate, r_v for H2C-SVLIF assuming an ν_d =85% duty cycle and using the maximum frame rates for a *Phantom* V2512 camera at the specified resolutions.

volumetric spatial resolution	r_f (Hz)	r_v (Hz)
384 × 384 × 384	117,117	129
512 × 512 × 512	75,669	62
640 × 640 × 640	52,974	35
768 × 768 × 768	39,180	21
1024 × 768 × 768	31,815	17
1280 × 800 × 800	25,722	13

4 File formats and viewing software

One of the challenges presented by volumetric imaging is the large data sets produced by the method. For example, 10 seconds of 512^3 volumes recorded at 100 vol/s results in a 134 GB of data (assuming 8-bit data storage). This data can be compressed, though for scientific analysis it should be done using a lossless method. Also, ideally the data would be capable of being decompressed fast enough for real-time viewing. This is a difficult constraint: playback at 30 volumes per seoncd would require a decompression speed of 4 GB/s (as measured in the decompressed data).

In a typical experiment a large fraction of the image volume is empty (i.e. containing no dye). In practice, this can range from 50–95% of the image voxels. In order to facilitate compression, we clip all pixel values below a certain threshold, chosen to eliminate the dark noise but have minimal impact on the collected data. After this clipping, the image volumes contain large contiguous regions of zeros which can be easily compressed. We use the LZ4 algorithm for data compression, which is extremely fast for both compression and decompression, and is supported by the widely used VTK data format (Schroeder (2006)). Our data is stored as VTK Image Files (VTI) which can be viewed in Paraview (Ahrens et al (2005)) and other software which supports the VTK pipeline.

Additionally, the VTK format allows us to include additional metadata about the volumes (physical dimensions, distortion correction information, etc.) which is ignored by third party software. This meta-data is used by our custom open source multi-scale ultra-fast volumetric imaging (MUVI) software, which is able to correct for volume distortions and playback the acquired videos at high rates with relatively modest hardware. This software, which was developed as part of the MUVI Lab at UC Merced, is also capable of dynamically display other 3D data including derived flow fields (see for example Fig. 8). The entire software package is open source and available on GitHub (Kleckner (2021b)).

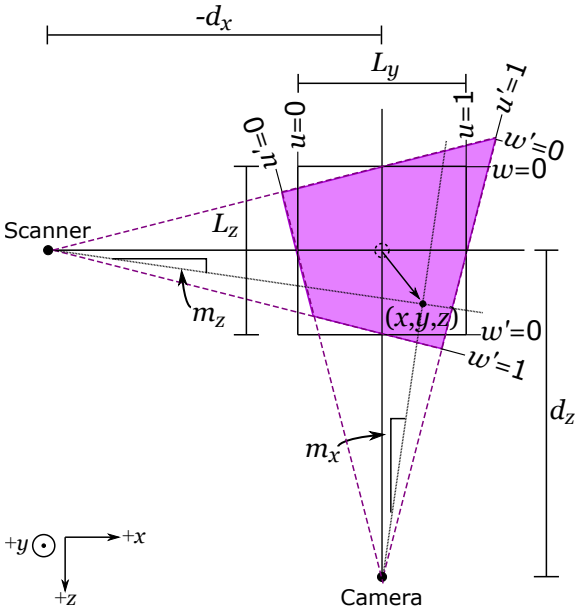

Fig. 4 Schematic of the coordinates used in distortion correction. The purple area indicates the raw distorted image space, the square black line shows the idealized image space, without distortion. Note that the sign of d_x and d_z depends on the location of the scanner and camera with respect to the volume. In the example shown above, the scanner is displaced in the negative x direction, so d_z is negative.

5 Post-processing

The volume imaged by the high-speed camera and scanning system is subject to distortion due to the viewing angle of the camera and the scan as seen in Fig. 1. Thus, the raw data obtained by our 3D imaging system includes distortion due to the varying angle of the laser sheet and the perspective distortions from the camera lens. Although in principle this could be corrected with optics (i.e. using a telecentric lens), this significantly complicates the experimental design and, in practice, limits the volume size. As an alternative, we have developed methods for correcting the resulting distortion in real-time display of the volumes, as well as in post-processing of the resulting data. This is enabled through our customized viewing software (MUVI) presented in Section 4.

5.1 Distortion correction

To correct the perspective, we use the following coordinate systems and transformations between them (Fig. 4):

- **Raw space coordinates:** Each point is assigned a coordinate (u', v', and w') in the range of 0–1, based on the relative position of each voxel along each axis in the recorded data.
- **Slope space coordinates:** Due to the nature of the imaging system, u', v', and w' correspond to *slopes* in physical space, rather than displacements. Note that, in the case of the laser scanner this 'slope' actually refers to an angle, but the difference is negligible (less than 1%) if the maximum angle is less than $\approx 10°$. The relationship between raw coordinates and the slopes is given by:

$$u' = \left(\frac{d_z}{L_x} m_x + \frac{1}{2}\right) \tag{4}$$

$$v' = \left(\frac{d_z}{L_y} m_y + \frac{1}{2}\right) \tag{5}$$

$$w' = \left(\frac{d_x}{L_z} m_z + \frac{1}{2}\right). \tag{6}$$

- **Physical coordinates:** We can compute the slope space coordinates in relation to physical space coordinates (x, y, and z) using the equations:

$$m_x = \frac{x}{d_z - z} \tag{7}$$

$$m_y = \frac{y}{d_z - z} \tag{8}$$

$$\tan(m_z) \approx m_z = \frac{z}{d_x - x}. \tag{9}$$

- **Idealized image coordinates:** It is also useful to define idealized image coordinates (u, v, and w) in an *undistorted* space:

$$x = \left(u - \frac{1}{2}\right) L_x \tag{10}$$

$$y = \left(v - \frac{1}{2}\right) L_y \tag{11}$$

$$z = \left(w - \frac{1}{2}\right) L_z. \tag{12}$$

  The limits of these coordinates extend slightly beyond the range 0 to 1 because of the mismatch between the non-rectilinear imaged space and the rectilinear idealized space (i.e. the extent to which the purple box in figure 5 extends beyond the black outline).

From these definitions, we can relate the raw image coordinates to the idealized image coordinates:

$$u' = \frac{u + \epsilon_z}{1 + 2\epsilon_z} \tag{13}$$

$$v' = \frac{v + \epsilon_z}{1 + 2\epsilon_z} \tag{14}$$

$$w' = \frac{w + \epsilon_x}{1 + 2\epsilon_x} \tag{15}$$

where:

$$\epsilon_z \equiv \frac{L_z}{4d_z}(1 - 2w) \tag{16}$$

$$\epsilon_x \equiv \frac{L_x}{4d_x}(1 - 2u)\,. \tag{17}$$

It is also possible to reverse this transformation:

$$u = \frac{u' + \epsilon'_z(2u' - 1 - 2\epsilon'_x)}{1 - 4\epsilon'_x\epsilon'_z} \tag{18}$$

$$v = \frac{v' + \epsilon'_z(2v' - 1 - 2\epsilon'_x)}{1 - 4\epsilon'_x\epsilon'_z} \tag{19}$$

$$w = \frac{w' + \epsilon'_x(2w' - 1 - 2\epsilon'_z)}{1 - 4\epsilon'_x\epsilon'_z} \tag{20}$$

where:

$$\epsilon'_x \equiv \frac{L_x}{4d_x}(1 - 2u') \tag{21}$$

$$\epsilon'_z \equiv \frac{L_z}{4d_z}(1 - 2w') \tag{22}$$

Although in principle the volumes could be perspective corrected before viewing and analysis, this would either result in image degradation or require up-scaling of the data. Both are highly undesirable. As a result, we have developed viewing software which corrects the perspective as it is being displayed. This works by converting the raw image coordinates into the idealized image coordinates using the equations above. As the transformation is relatively simple, this can be done at a low level in the display pipeline with minimal impact on performance.

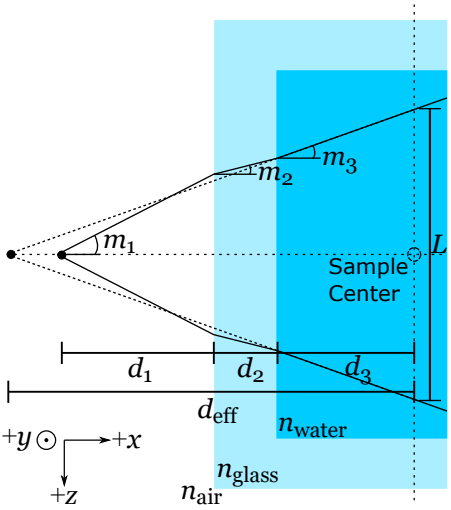

Fig. 5 Schematic of effective distance, d_{eff}, relative to the scanner. The effective distance is given by the distance from the center of sample to where the rays in the sample would have converged neglecting the refraction of the interfaces.

The distortion also needs to be corrected for any features extracted from the raw volume data. For example, consider the problem of particle tracking: if the raw volumes are sent to particle identification software, it will return their positions in the raw image space. These positions can then be converted to the idealized image space after the particle identification. The software library also provides built-in functions for this coordinate transformation.

5.2 Effective distance

The distortion correction discussed in the previous section assumes that the imaged volume has the same index of refraction as medium surrounding the scanning head and camera. For typical experiments, however, the imaged volume will be in a fluid, and so the deflection of the light rays by the dielectric interfaces need to be accounted for. In practice, this means that the distances,

d_x and d_z, from the sample center to the scanner head and from the sample center to the camera needs to be replaced with an effective distance, d_{eff}, accounting for the changing index of refraction, see Fig. 5.

The relationship between the maximum ray slopes, m_i, in different layers (e.g., air, glass, and water) is given by Snell's law (Jenkins and White (2001)), and applying the small angle approximation results in,

$$m_i = \frac{n_j}{n_i} m_j, \tag{23}$$

where n_i is the index of each layer. This relationship can be derived from Snell's law assuming the light rays are nearly perpendicular to all surfaces.

Thus, for a total of K interfaces,

$$\frac{L}{2} = \sum_{i=1}^{K} m_i d_i = n_K m_K \sum_{i=1}^{K} \frac{d_i}{n_i}, \tag{24}$$

and therefore,

$$d_{\text{eff}} = \frac{L}{2m_K} = n_K \sum_{1}^{K} \frac{d_i}{n_i}, \tag{25}$$

where n_K is the index of the final layer (i.e. $n_K = n_s$ is the index of the imaged volume). This effective distance can be used if layers are measured directly.

5.3 Calibration

We have also developed a process for automating the determination of parameters, L_x, L_y, L_z and d_x, d_z, using a calibration target. The target is composed of a regular grid of fluorescent spots, spaced by 5 mm, on a flat sheet of acrylic. The target is created from a sheet of 6 mm thick orange fluorescent acrylic, painted black on one side. A laser engraving system is used to engrave a rectangular grid of 1 mm spots, removing the black paint in these areas and exposing the fluorescent plastic underneath.

The distortion correction parameters, L_x, L_y, L_z and d_x, d_z, can be obtained directly from the raw distorted volumes of the grid captured by the camera. The process of obtaining the distortion correction parameters is as follows:

1. Image the target in the sample fluid, placed at an approximately 45° angle with respect to the camera so that the laser scanner can illuminate it entirely while also being fully visible to the camera.
2. Locate the centers of each spot in raw space coordinates using a particle tracking algorithm (see Section 6).
3. Construct a model which transforms from the positions on the target to the raw space coordinates, including distortion corrections, using Eqns. 18

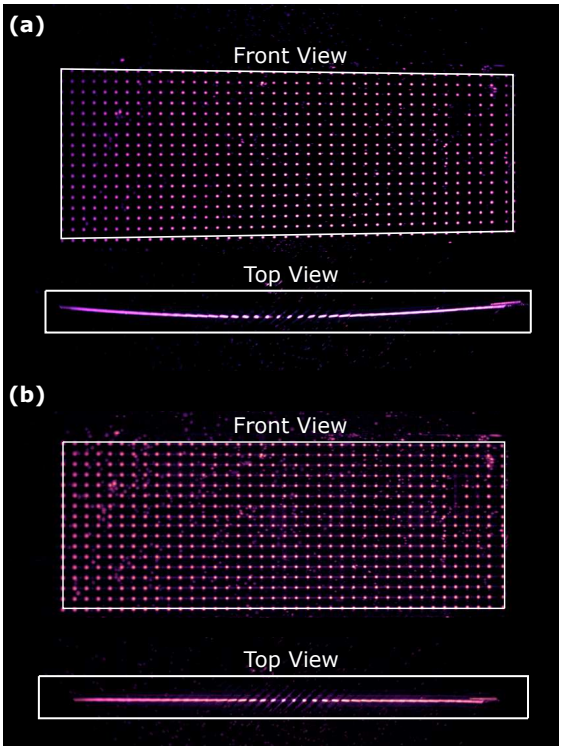

Fig. 6 Calibration target displayed in MUVI software. (**a**) Raw image data capture by the camera, without correction for perspective. (**b**) The same data after perspective correction.

- 22. This model incorporates L_x, L_y, L_z and d_x, d_z as well as arbitrary displacements and rotations of the target (modeled as Euler angles).

4. Optimize the parameters of this model using the Broyden–Fletcher–Goldfarb–Shanno algorithm (Nocedal and Wright (2006)). We minimize the following egg-crate fitness function:

$$U = -\cos^2\left(\frac{\pi x'}{s}\right)\cos^2\left(\frac{\pi y'}{s}\right) + \left(\frac{\pi z'}{s}\right)^2, \tag{26}$$

where $s = 5$ mm is the known distance between target points, and x', y', and z' are physical space coordinates of the tracked points after applying the transformation model in the previous step.

Fig. 6 shows an actual captured image of a calibration target before and after the perspective correction. We compute the RMS between the tracked points and the reconstructed points of our model, and find it to be within subvoxel accuracy, RMS ≈ 0.23 voxels.

6 Velocity measurements

In order to measure the velocity of the fluid, we use a particle tracking velocimetry (PTV) approach which locates individual tracer particles in the 3D volumes and links them into tracks over time. We then use a resampling algorithm to interpolate these tracks into smooth particle velocities, and a second algorithm to interpolate these discrete velocities onto an arbitrary regular grid. We note that if desired, it would also be possible to perform 3D PIV to obtain a velocity field (for example using OpenPIV; Liberzon et al (2020)). However, for the example cases presented below, it is possible to resolve individual tracer particles, so a particle tracking method is preferred.

We use an open-source library, *Trackpy* (Allan et al (2016)) for particle identification and tracking from volume to volume. *Trackpy* is an implementation of the Crocker-Grier algorithm (Crocker and Grier (1996)), which works by finding local peak intensities in the volumes. After localizing the peak intensities, the algorithm finds the positions of the particles by taking the average position of the pixels for which the particles spans and weights them by the brightness to locate their center of mass. After recovering the positions of the particles, we update the image coordinates of the particles to physical space coordinates using the distortion parameters, as discussed in Section 5.3.

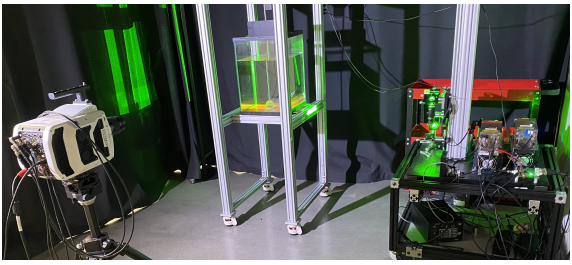

Fig. 7 A photograph of the experimental setup. In view are the imaging apparatus consisting of a high-speed camera (left), the experiment (center), and the laser sheet generator (right).

Under optimal scenarios the Crocker-Grier algorithm can return particle locations with sub-voxel accuracy, although in practice this is not always the case. The phenomenon of pixel locking, caused by experimental constraints, can lead to erratic trajectories that need to be smoothed. This is particularly relevant if the particle size is less than the imaged voxel size, which will likely be true for H2C-SVLIF. To smooth out the trajectories, we implement a modified Savitzky-Golay filter (Savitzky and Golay (1964)), which fits a 15 point window around each measurement to a second order polynomial. The "modified" part of the filter includes the ability to smooth trajectories of particle tracks with a small number of missing frames. This filter returns a new list of particle locations and velocities, giving us a randomly-spaced velocity

field measurement of the fluid. The complete implementation of this method is included in the MUVI software (Kleckner (2021b).)

To resample the velocity obtained at our randomly seeded particle locations to a regular grid, we implement a seconder order windowed polynomial fit in three spatial coordinates (Parviz and Moin (2008)). One advantage of this method is one can also compute the strain tensor or vorticity from the derivatives of the polynomial fit (Kambe (2007)). In practice, we select a radial cosine window as the weight function, $w(r) = \frac{1}{2}(1 + \cos \frac{\pi r}{a_0})$, and apply a least squares fit for smoothing (Geçkinli and Yavuz (1981)). The size of the interrogation window is set to $a_0 = 3\bar{r}$, where $\bar{r}$ is the median particle spacing; $\bar{r} =$ 3–5 mm for the experiments outlined in Section 7. This window size is selected such that, on average, there are 3.6 times more measured particle velocities than fit parameters. If desired, this size can be reduced to improve the spatial resolution of the results at the expense of an increase in noise sensitivity.

To eliminate the effect of spurious trajectories that sometimes result from errors in the linking stage, we first implement the windowed polynomial interpolation scheme on the sparse grid and interpolate the data back onto itself. This allows us to calculate the relative error between the interpolated velocities and the data; we then discard the worst 5% of particles. From the remaining trajectories, we reapply the windowed polynomial interpolation scheme to compute the velocity and vorticity on a regular grid.

Without modification, the effectiveness of this interpolation scheme is diminished near physical boundaries which reduce the number of measured particles in the fit window. In situations where these boundaries are at known locations and speeds – as in the experimental examples described below – this can be mitigated by inserting artificial tracer particles on the boundary which move at the boundary speed. In order to avoid biasing the resampling algorithm, we set the spacing of particles on the surface equal to the mean particle spacing. This scheme significantly improves the quality of the velocity measurements near the boundaries.

7 Results

We present two different sets of experiments to demonstrate our H2C-SVLIF imaging technique: (1) flow past a sphere with simultaneous measurement of tracer particles and a passive tracer and (2) laminar pipe flow with streamwise vortices embedded with dye. Although the second experiment only uses a single fluorescent channel, it uses most of the same hardware and identical software to extract two types of data from a single channel. In both cases, we collect PTV data to reconstruct the velocity and vorticity field. Dye is used to reveal different flow patterns in each of the experiments.

7.1 H2C-SVLIF

To validate our novel H2C-SVLIF technique, we designed a test experiment consisting of a 50 mm sphere pulled through a tank of water using a linear

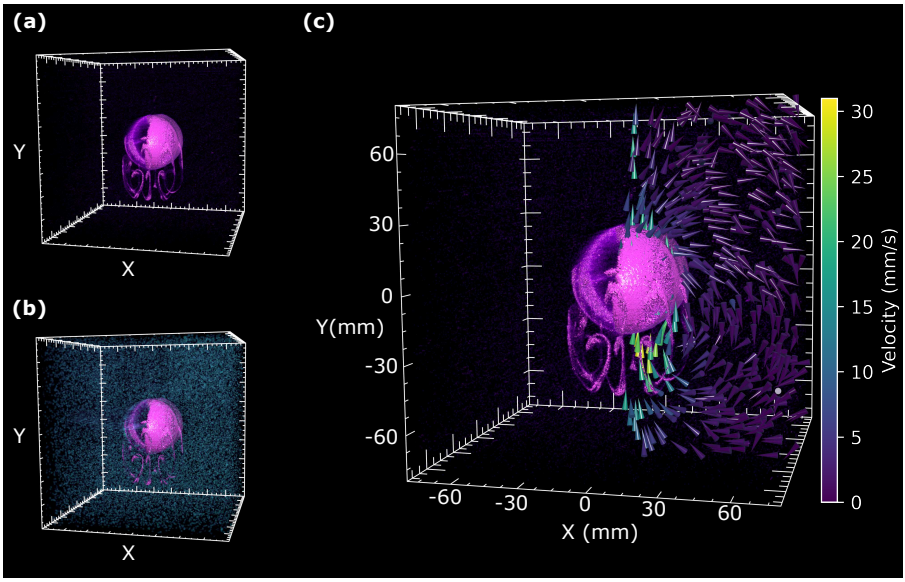

Fig. 8 Raw and processed data, imaged in the MUVI viewer software. **(a)** An isosurface of the UV dye channel, showing the sphere and the fluid shed from the dye injection points on the equator. **(b)** An overlay of the 3D tracer particle data (teal, obtained from the green excited dye channel). **(c)** An overlay of some of the velocities measured from tracer particles (purple to yellow arrows).

actuator (Fig. 7 and Supplementary Movie S1). We accelerate the sphere from rest to 18.8 mm/sec at a rate of 3.8 mm/s^2. The fluid is randomly seeded with neutrally buoyant tracer particles (*Cospheric* Orange Polyethylene Microspheres with 106-125 μm diameter); the number density is chosen so that they have an average spacing of $\bar{r} \approx 5$ mm. Their fluorescent absorption is well matched to the 532 nm laser (peak absorption: 530 nm, peak emission: 450 nm). A 532 nm dielectric laser notch filter is placed in front of the camera lens to block any light directly reflected from the sphere or other parts of the apparatus (i.e. so that we only image the fluorescent light).

The sphere is suspended vertically by a 9 mm diameter stainless steel tube, through which we inject fluorescent dye into channels on the equator of the sphere using a syringe pump located above the sample. The dye is a solution of 140 μmol/L coumarin dye (*Thermo Scientific Chemicals* Coumarin 2) in pure water. The absorption maximum of dye occurs at 370 nm, and is well matched to the 355 nm laser.

Table 3 summarizes all of the relevant experimental parameters. Note that to improve the SNR of the UV excited dye we use a larger aperture of f/2.8. Although this sacrifices some resolution near the edges of the sample, these regions primarily contain only tracer particles. Fortunately, spreading the intensity of a single tracer particle over several pixels should actually *improve* the particle tracking accuracy (Crocker and Grier (1996)).

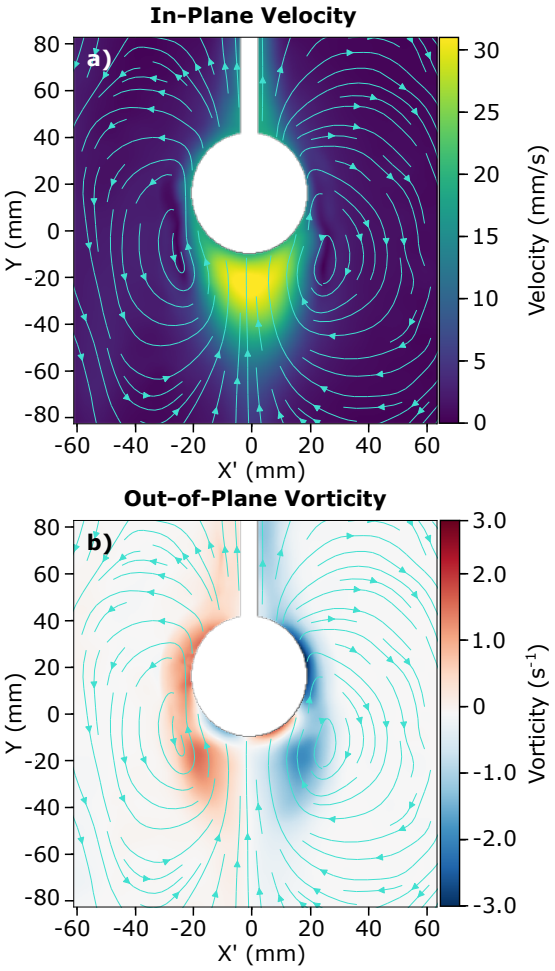

Fig. 9 **(a)** The in-plane velocity field and **(b)** out-of-plane vorticity field are plotted for a vertical slice of the volume at $L_z = -1.8$, and rotated about the y-axis by -40°. Streamlines are plotted to reveal flow patterns near the sphere.

3D reconstructed images of the dye shed from the sphere and the reconstructed flow field is shown in Fig. 8. According to previous studies (Spietz et al (2017); Sansica et al (2018)), vortex rings should be observed to be shed from the surface of the sphere for the Reynolds number used in the experiments, $Re = 950$. This can be readily seen in the data, as displayed in our custom-built software (Fig. 8 and Supplementary Movie S2). We can also construct a regularly sampled velocity field by interpolating the PTV velocity tracks using a windowed polynomial fit, as discussed in Section. 6. 2D slices of the velocity and vorticity field are shown in Fig. 9 (a vertical slice) and Fig. 10 (a horizontal slice).

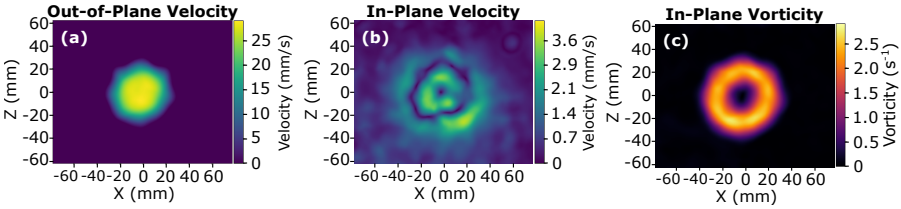

Fig. 10 **(a)** The out-of-plane velocity field, **(b)** the in-plane-velocity field, and **(c)** the in-plane vorticity field are plotted for a horizontal slice near the bottom of the sphere at $L_y = -18$. The in-plane velocity field reveals the core of a vortex ring, and the in-plane vorticity field reveals the corresponding vortex ring that is shed from the surface of the sphere.

Values	Definitions
140 μmol/L	Coumarin dye concentration
$\bar{r} \approx 5$ mm	Mean tracer particle spacing
14.5 mL/min	Dye injection rate
$u = 18.8$ mm/s	Sphere final velocity
$D = 50$ mm	Sphere diameter
$Re = \frac{uD}{\nu} = 950$	Reynolds number
$F = 2.8$ (f/2.8)	Lens aperture
$L_x = L_y$ =175.6 mm	Imaged volume size in x and y
$L_z = 143.3$ mm	Imaged volume size in z
$d_x = 1278$ mm	Effective distance from camera nodal point to center of volume
$d_z = 1822$ mm	Effective distance from scanning-head-platform to center of volume
$r_v = 65.1$ Hz	Volumetric acquisition rate
$N_x \times N_y \times N_Z = 512 \times 512 \times 512$	Volumetric spatial resolution

Table 3 The parameters used for flow past a sphere and conducting measurements using H2C-SVLIF.

7.2 One-Color SVLIF

In situations where image features are sufficiently different in geometry or brightness, multiple data streams can be obtained from a single fluorescent channel. This is desirable because it drastically reduces the complexity and size of the setup, and is adequate for many flows of interest. As an example to demonstrate this technique, we present high-speed volumetric imaging of stream-wise vortices embedded in laminar pipe flow.

Although the same H2C-SVLIF laser scanning head can be used in single channel mode, here we use a smaller, cheaper, and lighter system which can easily be integrated onto the moving carriage (Fig. 11). We note, however, that this system uses an identical camera and synchronization board as well as the same software to control the scanner and image the resulting data. All the optics for this experiment are mounted onto a breadboard that is itself mounted

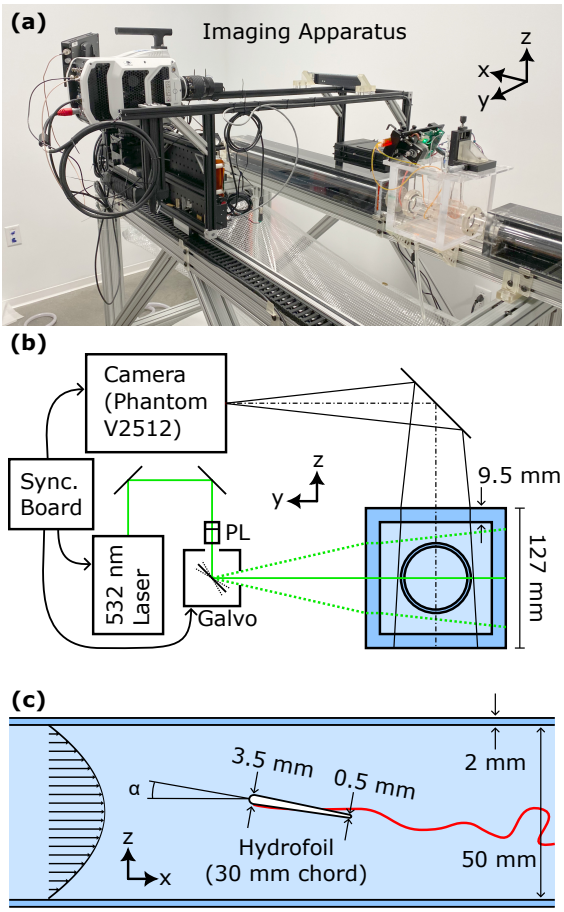

Fig. 11 **(a)** Experimental setup investigating vortex line instabilities in transitional pipe flow using single-color SVLIF. **(b)** The region of interest is contained in an acrylic box in order to submerge the quartz pipe in index-matched fluid. **(c)** Within the pipe, the wing is held in place with stainless steel tubes that inject Rhodamine 6G dye into channels to image vortex cores downstream.

onto a moving carriage that follows the flow in the pipe. The laser used is a diode-pumped pulsed laser (*Spectra Physics* Explorer One HE 532-200).

The flow under investigation is created by injecting two counter-rotating vortices into a laminar background pipe flow. (Experimental parameters are listed in Table 4.) The vortices are generated by a small hydrofoil placed in the pipe; the resulting vortices are made visible by injecting dilute Rhodamine 6G through slots in the leading edge (Fig. 11**c**). The pipe is held in place by an acrylic box for the purpose of submerging the pipe in index-matched fluid (water), and providing stability to the tube (Fig. 11**b**). The qualitative appearance of these dyed vortex cores appears as two bright lines spanning the frame, allowing us to track them precisely using the Fast Marching Method (Fig. 12**(a-b)**; Sethian (1999), Kleckner and Irvine (2013)).

Values	Definitions
250 μmol/L	Rhodamine 6G dye concentration
0.025 mL/min	Dye injection rate
$\bar{r} = 3.0$ mm	Median particle spacing
$D = 50$ mm	Pipe diameter
$Re = \frac{\bar{u}D}{\nu} = 1023$	Reynolds number
$F = 22$ (f/22)	Lens aperture
$L_x = 294.1$ mm	Imaged volume size (stream-wise) in x
$L_y = 69.9$ mm	Imaged volume size in y
$L_z = 54.0$ mm	Imaged volume size in z
$d_x = 1264.7$ mm	Effective distance from camera nodal point to center of volume
$d_z = 660.3$ mm	Effective distance from scanning-head-platform to center of volume
$r_v = 34.8$ Hz	Volumetric acquisition rate
$N_x \times N_y \times N_Z = 1280 \times 304 \times 256$	Volumetric spatial resolution

Table 4 The parameters used for flow past a wing using single-color SVLIF.

One minor modification compared to the previous results is that the laser sheet generator is displaced along the y-axis as opposed to the x-axis as described above. As a result, the distortion correction uses a modified formula where $x \leftrightarrow y$, but which is otherwise identical. This imaging configuration was chosen to minimize the distance light travels through the sample for both the laser sheet and camera, improving imaging quality for this particular experiment.

In addition to the dyed vortices, we also include small tracer particles in the flow (*Cospheric* Orange Polyethylene Micro-spheres size 106-125 μm), with a mean particle spacing of $\bar{r} \approx 3.0$ mm. This allows for simultaneous measurement of the velocity field in the pipe (Fig. 12**(b-e)**). Table 4 summarizes the relevant experimental parameters for the experiment. The combined reconstruction technique allows for coarse resolution velocity fields (≈ 3 mm) to be measured at the same time as high resolution (≈ 1 mm) vortex line geometry (Supplementary Movie S3).

8 Conclusion

We have presented a novel H2C-SVLIF imaging technique which permits flexible high-speed volumetric imaging of multiple data channels in a fluid flow. This system is considerably faster than existing multi-channel volumetric imaging techniques; is capable of two channel speeds of up to 65 volumes per second at a resolution of 512×512×512. For demonstration purposes, we have employed the technique to image two different experiments using similar techniques and hardware. In addition to demonstrating the flexibility of our novel H2C-SVLIF technique, we provide a comprehensive discussion of the practical limits of the technique, including laser intensity, sample size/resolution, and

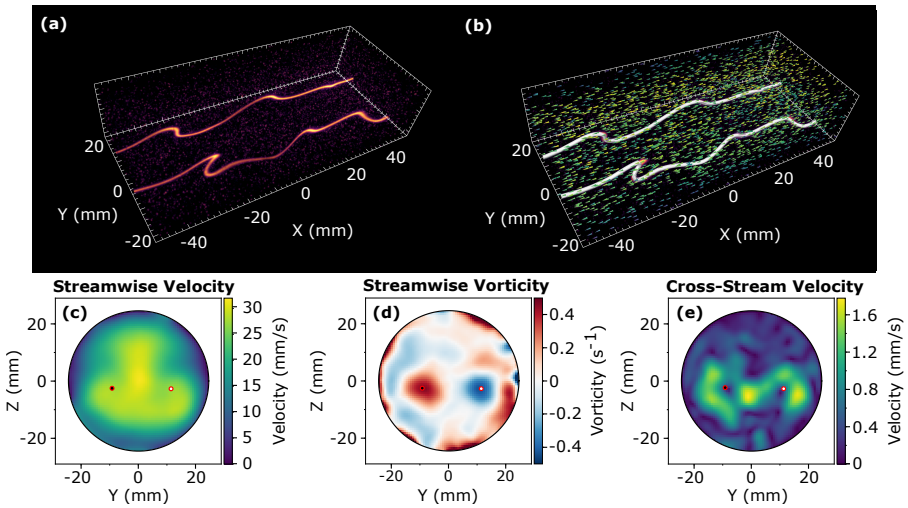

Fig. 12 **(a)** Example of raw data in MUVI volumetric viewer. **(b)** Vortex line tracking is used in conjunction with particle tracking to find vortex location and reconstruct trajectories around vortex lines superimposed onto raw data. These trajectories are used to reasmple select measurements onto a regular grid using a second-order polynomial fit, and are displayed in conjunction with vortex line locations, shown as white and black points outlined in red. **(c)** Streamwise velocity profile makes a distinct shape as vortices move slower moving fluid inward and faster moving fluid outward. **(d)** Streamwise vorticity profile shows vortices seeded by wing. **(e)** Cross stream velocity also follows vortex cores, shown as regions of higher velocity around vortex cores.

camera and scanning speed. We have also described fundamental limits to volumetric imaging, including both diffraction limits to resolution and the effects of shot noise to the SNR of the resulting images. All of these limits should apply not only to our experiments, but to any high-speed volumetric imaging using similar techniques.

Our system also includes open source software and hardware which simplifies and automates much of the data gathering, imaging, and processing. This includes automated correction of perspective distortion effects using a calibration target and real time playback and manipulation of the resulting data which incorporates these corrections. By integrating the ability to correct for distortion effects we considerably simplify the experiment setup, which would otherwise require large and complicated optics to produce rectilinear imaging.

The test experiments presented in this manuscript demonstrate simultaneous visualisation of the reconstructed velocity tracks and dyed regions of fluid. This demonstrates the ability to reconstruct multiple high-speed data streams in 3D from a single experiment, using either 2 channel imaging or by reconstruction of geometrically distinct features in a single channel. The flexibility of the technique allows it to be applied to a wide range of systems for high-speed single shot measurements.

9 Declarations

9.1 Ethical approval

Not applicable.

9.2 Competing interests

The authors declare they have no competing financial interests.

9.3 Authors' contributions

D.K. and S.K. conceived the 3D imaging concept, acquired funding, and advised D.T.S., T.M., and C.C. on its implementation. D.T.S., C.C., T.M. and D.K. designed and constructed the imaging apparatus and wrote the associated imaging software. D.T.S. and C.C. conducted the demonstration experiments and data analysis. D.T.S., S.K., D.K., and C.C. wrote the main manuscript text. D.K. prepared figure 1. D.T.S. prepared figures 2-10. C.C. prepared figures 11-12. All authors reviewed the manuscript.

9.4 Funding

Funding for this research was provided by the the Department of Defense, Defense University Research Instrumentation Program awarded by the Army Research Office, Award Number W911NF-19-1-0215.

9.5 Availability of data and materials

The 3D imaging software and designs for the synchronizer board are open source and publicly available (Kleckner (2021b); Kleckner (2021a)). The data from the example experiments shown in the paper is available by request.

References

Adamczyk AA, Rimai L (1988) 2-Dimensional particle tracking velocimetry (PTV): Technique and image processing algorithms. Experiments in Fluids 6(6):373–380. https://doi.org/10.1007/BF00196482

Ahrens J, Geveci B, Law C (2005) Paraview: An end-user tool for large data visualization

Allan D, Caswell T, Keim N, et al (2016) trackpy: Trackpy v0.3.2. https://doi.org/10.5281/zenodo.60550, URL https://doi.org/10.5281/zenodo.60550

Brücker C, Althaus W (1992) Study of vortex breakdown by particle tracking velocimetry (PTV). Experiments in Fluids 13(5):339–349. https://doi.org/10.1007/BF00209508

Bryanston-Cross P, Epstein A (1990) The application of sub-micron particle visualisation for PIV (Particle Image Velocimetry) at transonic and supersonic speeds. Progress in Aerospace Sciences 27(3):237–265. https://doi.org/10.1016/0376-0421(90)90008-8

Cornic P, Leclaire B, Champagnat F, et al (2020) Double-frame tomographic PTV at high seeding densities. Experiments in Fluids 61(2):23. https://doi.org/10.1007/s00348-019-2859-2

Crocker JC, Grier DG (1996) Methods of Digital Video Microscopy for Colloidal Studies. Journal of colloid and interface science 179(1):298–310. https://doi.org/10.1006/jcis.1996.0217

Flammang BE, Lauder GV, Troolin DR, et al (2011) Volumetric imaging of shark tail hydrodynamics reveals a three-dimensional dual-ring vortex wake structure. Proceedings of the Royal Society B: Biological Sciences 278(1725):3670–3678. https://doi.org/10.1098/rspb.2011.0489

Geçkinli NC, Yavuz D (1981) A set of optimal discrete linear smoothers. Signal processing 3(1):49–62. https://doi.org/10.1016/0165-1684(81)90064-5

Gerrard A, Burch JM (1994) Introduction to Matrix Methods in Optics. Courier Corporation

Gilroy K, Lucatorto T (2019) Overcoming Shot Noise Limitations in High Speed Imaging with Bright Field Mode

Halls BR, Hsu PS, Roy S, et al (2018) Two-color volumetric laser-induced fluorescence for 3D OH and temperature fields in turbulent reacting flows. Optics Letters 43(12):2961. https://doi.org/10.1364/OL.43.002961

Hammack SD, Carter CD, Skiba AW, et al (2018) 20 kHz CH_2O and OH PLIF with stereo PIV. Optics Letters 43(5):1115. https://doi.org/10.1364/OL.43.001115

HONG Z, ZHENG H, CHEN J, et al (2001) Laser-diode-pumped Cr4+, Nd3+:YAG self-Q-switched laser with high repetition rate and high stability. Applied physics B, Lasers and optics 73(3):205–207. https://doi.org/10.1007/s003400100641

Janesick JR (2007) Photon Transfer. SPIE, Bloomington

Jenkins FA, White HE (2001) Fundamentals of Optics. McGraw-Hill, New York; Montreal

Kambe T (2007) Elementary Fluid Mechanics. World Scientific, Hackensack, N.J. ; London

Katija K, Colin SP, Costello JH, et al (2015) Ontogenetic propulsive transitions by Sarsia tubulosa medusae. Journal of Experimental Biology 218(15):2333–2343. https://doi.org/10.1242/jeb.115832

Kleckner D (2021a) Kleckner lab github repository: Analog-digital synchronization board schematics. https://github.com/klecknerlab/ad_sync

Kleckner D (2021b) Kleckner lab github repository: Muvi lab 3d imaging library. https://github.com/klecknerlab/muvi

Kleckner D, Irvine WTM (2013) Creation and dynamics of knotted vortices. Nature Physics 9(4):253–258. https://doi.org/10.1038/nphys2560

Krug D, Holzner M, Lüthi B, et al (2014) A combined scanning PTV/LIF technique to simultaneously measure the full velocity gradient tensor and the 3D density field. Measurement Science and Technology 25(6):065,301. https://doi.org/10.1088/0957-0233/25/6/065301

Liberzon A, Lasagna D, Aubert M, et al (2020) OpenPIV/openpiv-python: OpenPIV - Python (v0.22.2) with a new extended search PIV grid option. https://doi.org/10.5281/zenodo.3930343, URL https://doi.org/10.5281/zenodo.3930343

Ma L, Lei Q, Ikeda J, et al (2017) Single-shot 3D flame diagnostic based on volumetric laser induced fluorescence (VLIF). Proceedings of the Combustion Institute 36(3):4575–4583. https://doi.org/10.1016/j.proci.2016.07.050

Meyer TR, Halls BR, Jiang N, et al (2016) High-speed, three-dimensional tomographic laser-induced incandescence imaging of soot volume fraction in turbulent flames. Optics express 24(26):29,547–29,555. https://doi.org/10.1364/OE.24.029547

Nocedal J, Wright SJ (2006) Numerical Optimization, second edition. edn. Springer Series in Operations Research and Financial Engineering, Springer, New York, NY, https://doi.org/10.1007/978-0-387-40065-5

Ortiz-Dueñas C, Kim J, Longmire EK (2010) Investigation of liquid–liquid drop coalescence using tomographic PIV. Experiments in Fluids 49(1):111–129. https://doi.org/10.1007/s00348-009-0810-7

Osborne JR, Ramji SA, Carter CD, et al (2016) Simultaneous 10 kHz TPIV, OH PLIF, and CH2O PLIF measurements of turbulent flame structure and dynamics. Experiments in Fluids 57(5):65. https://doi.org/10.1007/s00348-016-2151-7

Ouellette NT (2012) Turbulence in two dimensions. Physics Today 65(5):68–69. https://doi.org/10.1063/PT.3.1570

Palafox P, Oldfield MLG, LaGraff JE, et al (2007) PIV Maps of Tip Leakage and Secondary Flow Fields on a Low-Speed Turbine Blade Cascade With Moving End Wall. Journal of Turbomachinery 130(1). https://doi.org/10.1115/1.2437218

Parviz M, Moin MS (2008) Multivariate Polynomials Estimation Based on GradientBoost in Multimodal Biometrics. In: Advanced Intelligent Computing Theories and Applications. With Aspects of Contemporary Intelligent Computing Techniques. Communications in Computer and Information Science, Springer Berlin Heidelberg, Berlin, Heidelberg, p 471–477, https://doi.org/10.1007/978-3-540-85930-7_60

Pepper RE, Jaffe JS, Variano E, et al (2015) Zooplankton in flowing water near benthic communities encounter rapidly fluctuating velocity gradients and accelerations. Marine Biology 162(10):1939–1954. https://doi.org/10.1007/s00227-015-2713-x

Samson JE, Miller LA, Ray D, et al (2019) A novel mechanism of mixing by pulsing corals. Journal of Experimental Biology 222(15). https://doi.org/10.1242/jeb.192518

Sansica A, Robinet JC, Alizard F, et al (2018) Three-dimensional instability of a flow past a sphere: Mach evolution of the regular and Hopf bifurcations. Journal of fluid mechanics 855:1088–1115. https://doi.org/10.1017/jfm.2018.664

Savitzky Abraham, Golay MJE (1964) Smoothing and Differentiation of Data by Simplified Least Squares Procedures. Analytical Chemistry 36(8):1627–1639. https://doi.org/10.1021/ac60214a047

Schroeder W (2006) The Visualization Toolkit: An Object-Oriented Approach to 3D Graphics, 4th edn. Kitware, New York

Sethian JA (1999) Fast Marching Methods. SIAM review 41(2):199–235. https://doi.org/10.1137/S0036144598347059

Shi S, Ding J, Atkinson C, et al (2018) A detailed comparison of single-camera light-field PIV and tomographic PIV. Experiments in Fluids 59(3):46. https://doi.org/10.1007/s00348-018-2500-9

Siegman Anthony E (1986) Physical Properties of Gaussian Beams. In: Lasers. University Science Books, p 1–1

Spietz HJ, Hejlesen MM, Walther JH (2017) Iterative Brinkman penalization for simulation of impulsively started flow past a sphere and a circular disc. Journal of Computational Physics 336:261–274. https://doi.org/10.1016/j.jcp.2017.01.064

Tropea C, Yarin AL, Foss JF (2007) Springer Handbook of Experimental Fluid Mechanics. Gale Virtual Reference Library, Springer, Berlin

Versluis M (2013) High-speed imaging in fluids. Experiments in fluids 54(2):1–35. https://doi.org/10.1007/s00348-013-1458-x

Ward P, Jacobson E (2000) Manual of Photography, ninth edn. Burlington: Focal Press

Wilga CD, Lauder GV (2002) Function of the heterocercal tail in sharks: Quantitative wake dynamics during steady horizontal swimming and vertical maneuvering. Journal of Experimental Biology 205(16):2365–2374. https://doi.org/10.1242/jeb.205.16.2365

Wilga CD, Lauder GV (2004) Hydrodynamic function of the shark's tail. Nature (London) 430(7002):850–850. https://doi.org/10.1038/430850a

Wu Y, Xu W, Lei Q, et al (2015) Single-shot volumetric laser induced fluorescence (VLIF) measurements in turbulent flows seeded with iodine. Optics Express 23(26):33,408. https://doi.org/10.1364/OE.23.033408

Zhu X, Sabatino DR, Rossman T (2019) 3D planar laser-induced fluorescence (PLIF) reconstruction of a hairpin vortex. In: AIAA

10 Supplementary information

Supplementary movie captions are provided in this section.

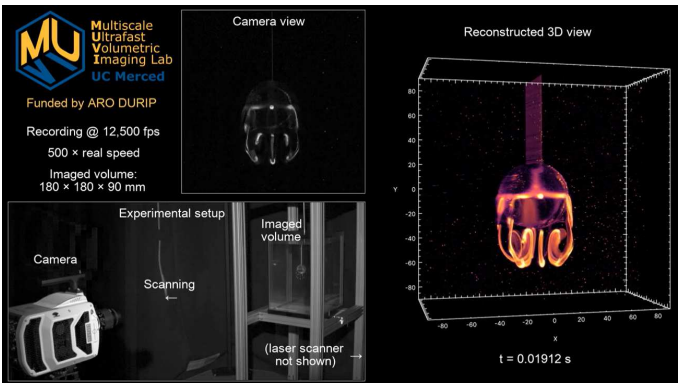

Fig. 13 Supplementary Movie S1. A movie displaying the experimental set up, the frames captured by the camera, and the reconstructed volumes.

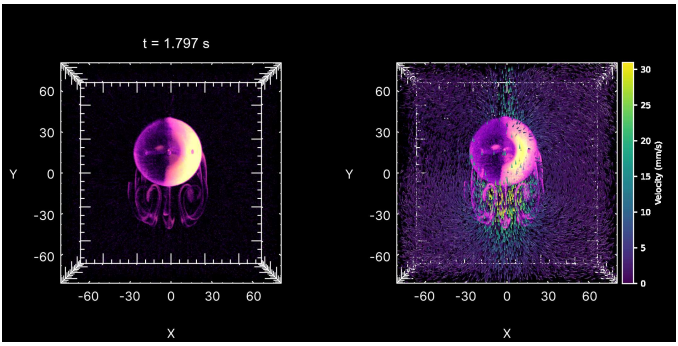

Fig. 14 Supplementary Movie S2. A movie of raw data of the embedded fluorescent dye (left), and the PTV velocity field superimposed with the fluorescent dye (right) for flow past a sphere.

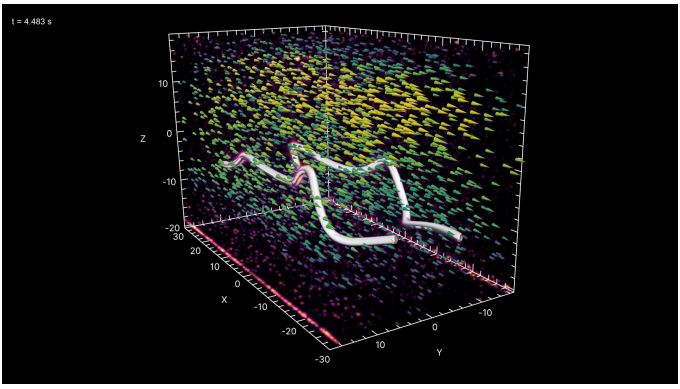

Fig. 15 Supplementary Movie S3.A movie of the vortex line tracking of the dye superimposed with PTV tracks for vortices in a pipe flow.

Supplementary Files

This is a list of supplementary files associated with this preprint. Click to download.

- MovieS1.mp4
- MovieS2.mp4
- MovieS3.mp4